Waiting time distributions in quantum spin Hall based heterostructures

F. Schulz,[1] D. Chevallier,[2] and M. Albert[3]
[1]*Department of Physics, University of Basel, Klingelbergstrasse 82, CH-4056 Basel, Switzerland*
[2]*Bleximo Corp., 701 Heinz Ave, Berkeley, California 94710, USA*
[3]*Université Côte d'Azur, CNRS, Institut de Physique de Nice, 06560 Valbonne, France*

(Received 10 October 2022; revised 22 April 2023; accepted 16 May 2023; published 5 June 2023)

We study the scattering processes and the associated waiting time distributions (WTDs) in heterostructures based on one-dimensional helical edge states of a two-dimensional topological insulator. In combination with a proximitized s-wave superconductor and an applied magnetic field a topological transition occurs. Along this transition the WTD reveals specific features related to the presence of Andreev bound states at finite energy or Majorana bound states at zero energy under ideal conditions. The effects of several imperfections such as disorder and finite temperature are discussed.

DOI: 10.1103/PhysRevB.107.245406

I. INTRODUCTION

The quest of Majorana fermionic states in condensed-matter physics, has been the subject of a strong interest during the past decades, in particular because of their exotic properties, such as non-Abelian statistics, that open the way to using them for quantum computation [1,2]. Among many proposals to create them, heterostructures based on two-dimensional topological insulators (TIs) are one interesting path of research. Previous investigations on the topologically nontrivial bulk band inversion in TIs result in quasi-one-dimensional TRS protected counterpropagating edge states [3–5]. While the band structure in quantum well systems is highly sensitive to its thickness, it remains challenging to handle the energetic localization of the Dirac point (DP) [6]. These spin-polarized states in combination with an s-wave superconductor (SC) and a magnetic field can be used to engineer Majorana bound states (MBSs) within different geometrical setups [7–10]. Induced superconductivity in the edge states of TIs has experimentally been realized in quantum well setups [11–18], or alternatively on thin-layer TIs [19–23]. The combination with a magnetic field for such systems results in a zero-energy mode in the conductance, potentially allowing the characterization of a MBS [24]. Topological superconductivity has also been realized in semiconducting nanowires [25–27] and has generated a lot of interest [28]. Usual conductance measurements to identify necessary characteristics of MBSs for such topological setups can be affected by the presence of trivial states [29–36], such that we are motivated for alternative measurements. One possibility would be to resort to the waiting time distributions (WTDs) [37–49], namely the distribution of time delay between the detection of two consecutive charge carriers, which has been shown to reveal traces of MBS in such nontrivial systems [46–48]. Whether this observable may provide a clear signature of the presence of a MBS is still under debate. However, the influence of the nature of different resonances in the scattering spectrum on waiting times is important and deserves to be addressed. Improving its understanding is the main purpose of this work.

Necessary techniques for the counting of single particles have become very precise, allowing a novel measurement for the processes of specific scattering events [49–58]. The resulting WTD in turn provides statistics including signatures that may help to distinguish between topologically trivial and nontrivial states within the system. WTDs in semiconducting hybrid systems have recently been studied, providing distinct features of a one-dimensional p-wave SC in comparison to an s-wave SC [46]. Further theoretical investigations have shown results for entangled electrons on a SC interface for MBSs [47,48].

In this paper we study WTDs in materials based on topological hybrid junctions as presented on Fig. 1. We combine the WTD as a statistical characterization tool to detect several transport effects that appear within such topological junctions. We unpack the complexity of the scattering processes involved in this setup by increasing smoothly its complexity until the topological phase transition is reached. This allows us to discuss features in the WTD related to the presence of finite energy ABSs or zero-energy MBSs in the setup under ideal conditions. These features are shown to be robust to the addition of several parasitic ingredients such as finite temperature and disorder in the system. However, spurious zero-energy resonances, such as trivial or partially separated ABSs, could mimic the effect of a MBS, although we have not been able to identify mechanisms to create them in TIs in this work. This clearly deserves further consideration.

The paper is set up as follows. In Sec. II we introduce the model that is used for the underlying N-S-F-S-N junction. In Sec. IV C we recap the substance of WTDs. The results are presented in Sec. IV, where we elaborate WTDs for specific types of hybrid quantum conductors, closely related to the Fu and Kane structure [8]. We study in detail the WTDs of different scattering processes in the presence of ABS or MBS and identify possible signatures to distinguish them. We finally discuss the effect of imperfections in the setup such as finite temperature and disorder. Conclusion and outlook are given in Sec. V and several technical details are available in Appendixes.

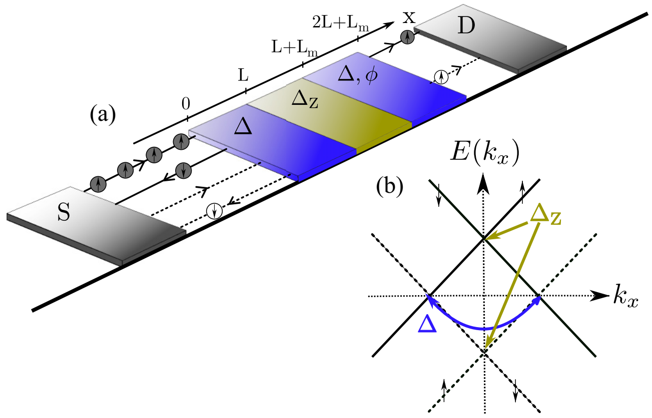

FIG. 1. (a) Schematic of the setup described by Eq. (1), containing counterpropagating one-dimensional edge states with two superconducting (blue) regions enclosing a ferromagnet (yellow) and connected to source and drain electrodes. Further indicated are the possible scattering states of an incoming spin up electron, which may be reflected as electron/hole (solid/dotted line) or be transmitted as electron/hole. (b) Energy spectra indicating the effective paring amplitudes in the scattering regions.

II. MODEL

The heterostructure we consider consists of helical counterpropagating edge states of a quantum spin Hall insulator, where only one edge is proximity coupled to a spatially restricted s-wave superconductor and a magnetic field [see Fig. 1(a)]. Similar setups have been studied in the literature [7,8,59–61]. In the basis $\Psi = (\psi_\uparrow, \psi_\downarrow, \psi_\uparrow^\dagger, \psi_\downarrow^\dagger)$, the Hamiltonian of the system under consideration is the following:

$$H = \begin{pmatrix} H_0 & H_{SC}^* \\ H_{SC} & -H_0^* \end{pmatrix}, \tag{1}$$

where $H_0 = H_{TI} + H_Z$. The Hamiltonian $H_{TI} = v_F k_x \sigma_3 - \mu$ is the kinetic term of the edge states, with Fermi velocity v_F ($\hbar = 1$), momentum $k_x = -i\partial_x$, chemical potential μ and spin quantization axis along the z direction, while $H_Z = \sigma_1 \Delta_Z(x)$ is the Zeeman field pointing in x direction. Furthermore, $H_{SC} = -i\Delta(x)\sigma_2$ includes the superconductor, which is assumed to be grounded, and the Pauli matrices σ (τ) act in spin (Nambu) space. The spatial arrangements of Δ and Δ_Z are chosen to have a ferromagnetic region enclosed by two superconducting regions, such that $\Delta(x) = \Delta[\Theta(x) - \Theta(x - L)] + \Delta e^{i\phi}[\Theta(x - L - L_m) - \Theta(x - 2L - L_m)]$ and $\Delta_Z(x) = \Delta_Z[\Theta(x - L) - \Theta(x - L - L_m)]$. The pairing mechanisms open a gap in the spectrum of the edge states [see schematic in Fig. 1(b)], which is either at the DP (Δ_Z) or at the Fermi level crossing (Δ). In addition we also assume a superconducting phase difference ϕ across the system [see Fig. 1(a)].

For our interests we study two cases. First, no Zeeman field is applied (trivial phase) and the middle region hosts freely propagating helical states, acting as a Fabry-Pérot interferometer [62]. Second, we include a finite Zeeman field, which couples the two spin species and opens a gap in the middle region, resulting in the emergence of zero-energy MBSs localized on the interfaces of the superconducting and magnetic regions [8]. This topological transition takes place above a certain threshold of the Zeeman field, which depends on the system parameters. The localization of the zero-energy MBSs arises due to domain walls with a different mass sign along the Jackiw-Rebbi model and decay with the inverse of the gap into the respective region. We check the characterization of different phases appearing in the heterostructure, by first presenting the scattering features as a basis to identify distinct signatures in the WTD. Whereby we use the seminal work of Blonder, Tinkham, and Klapwijk (BTK) to calculate the corresponding scattering coefficients [63]. We assume in this work a rather long junction ($L_m > v_F/\Delta$), such that for $\Delta_Z = 0$ multiple resonances are well defined within the superconducting gap $E < \Delta$ [see Fig. 2(a)]. Calculating the wave function with the continuity conditions on the interfaces at $x = 0, L, L + L_m$ and $x = 2L + L_m$ results in the necessary transport coefficients. With a preserved TRS ($\Delta_Z = 0$), an incoming right-moving electron from the source is protected from backscattering, such that there are only two nonvanishing processes. Namely, the cotunneling of an electron (t_e) form source to drain and the local Andreev reflection (r_h) on the SC interface at $x = 0$. The breaking of TRS in turn then also allows normal electron reflection (r_e), including a spin flip, and the transmission of holes (t_h). While the gap closing and reopening is usually used as an indicator of the topological phase transition, we use only the normal electron reflection signature, accompanied by its probability at zero energy from zero to one. Details are presented in Appendixes A and B. Based on those energy-dependent coefficients, we evaluate the corresponding WTDs, which we introduce in the next section.

III. WAITING TIME DISTRIBUTION

For the sake of clarity, we recap in this section the formalism used for the calculation of WTDs [37–40] as well as some well-established results that will serve as reference. The WTD $\mathcal{W}(\tau)$ denotes the probability distribution for the time delay τ between the detection of two consecutive charge carriers. They can be electrons or holes for instance. This quantities give precise and transparent information about correlations in a transport process. In general, it is customary to calculate it from the idle time probability (ITP) $\Pi(\tau)$, namely the probability to detect zero particles during a time interval τ. For stationary processes these two distributions are connected by the following expression:

$$\mathcal{W}(\tau) = \langle\tau\rangle \frac{\partial^2 \Pi(\tau)}{\partial \tau^2}. \tag{2}$$

For noninteracting systems, the ITP is given by the determinant formula [39]

$$\Pi(\tau) = \det(1 - Q_\tau), \tag{3}$$

where Q_τ is a projector over the time window τ whose expression depends on the detection scheme (measurement of consecutive electrons, holes, etc.) and the scattering matrix of the system. Explicit formulas are given below for the processes of interest. In addition, the mean waiting time is in general given by

$$\langle\tau\rangle = -\frac{1}{\dot{\Pi}(\tau = 0)}, \tag{4}$$

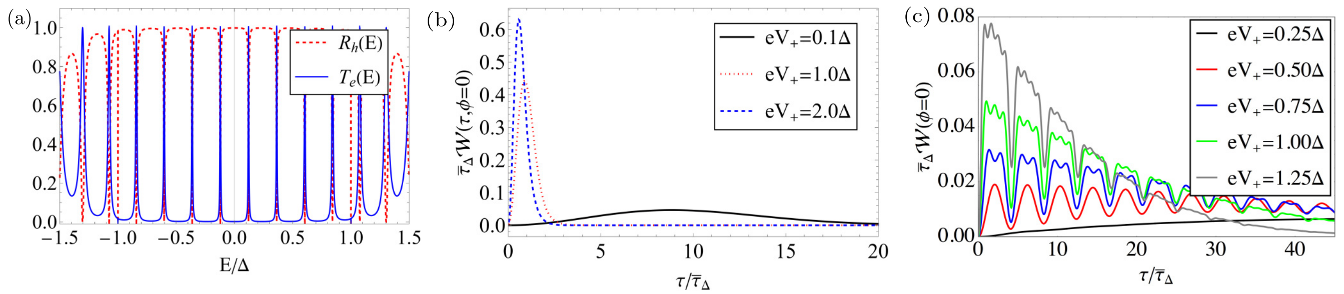

FIG. 2. (a) Energy dependence for the scattering coefficients $T_e(E)$ (blue) and $R_h(E)$ (red dotted) for $\phi = 0$ and $\Delta_Z = 0$. Resonances reflect ABS in the normal region. (b) WTD between holes (Andreev reflected electrons with $R_h(E)$) flowing back to the source for the indicated energy windows referring to (a). (c) WTD for transmitted electrons flowing to the drain. Each distribution covers an increasing number of resonances. The parameters are chosen to be $L = 2/\Delta$, $L_m = 6L$, $\Delta_Z = 0$.

with $\dot{\Pi}(\tau = 0) = \frac{\partial \Pi(\tau)}{\partial \tau}|_{\tau=0}$. To continue, we specify a detection procedure for the WTD. Thus, we calculate the ITP with the projection of a single-particle scattering state on a discrete voltage window around the Fermi level. In the range of the applied voltage V, the linear energy spectrum is discretized into N compartments with wave vectors $k = \frac{n}{N}\frac{eV}{\hbar v_F}$. A stationary process is then reached by the limit $N \to \infty$. We label the matrix elements of Q_τ with the four possible scattering processes as

$$\left[Q_\tau^{t_e}\right]_{\rm nm} \approx \frac{\kappa t_e(\kappa n) t_e^*(\kappa m)}{2\pi} K_\tau[\kappa(n-m)], \tag{5}$$

$$\left[Q_\tau^{t_h}\right]_{\rm nm} \approx \frac{\kappa t_h(\kappa n) t_h^*(\kappa m)}{2\pi} K_\tau[\kappa(n-m)], \tag{6}$$

$$\left[Q_\tau^{r_e}\right]_{\rm nm} \approx \frac{\kappa r_e(\kappa n) r_e^*(\kappa m)}{2\pi} K_\tau[\kappa(n-m)], \tag{7}$$

$$\left[Q_\tau^{r_h}\right]_{\rm nm} \approx \frac{\kappa r_h(\kappa n) r_h^*(\kappa m)}{2\pi} K_\tau[\kappa(n-m)], \tag{8}$$

where κ results from the discrete energy compartment to $\frac{1}{N}\frac{eV}{\hbar v_F}$ in the measured energy window eV and the kernel is given by

$$K_\tau[\kappa(n-m)] = \frac{2e^{-i\kappa(n-m)\frac{v_F\tau}{2}} \sin\left(\kappa(n-m)\frac{v_F\tau}{2}\right)}{\kappa(n-m)}. \tag{9}$$

Thus, we can measure the distribution of waiting times for outgoing electrons or holes from source to drain with Eq. (5) or Eq. (6). Similarly, with the assumption of a grounded superconductor, we calculate the WTDs of reflected electrons Eq. (7) or holes Eq. (8). The corresponding scattering coefficients, $t_{e/h}$ and $r_{e/h}$, are in general strongly energy dependent and can be seen as an energy filter within the transport window, which will be described later in the text. With this framework we are able to calculate the energy-dependent ITP from the determinant of the matrix in Eq. (3), needed for the WTD [Eq. (2)]. Depending on the point of interests, we focus in the next sections on specific scattering processes and their features appearing within the designated WTD.

Before going further in the analysis of our model, we first recall some important results that will be useful to understand our work. A reference case is the one of a single quantum channel subjected to a voltage eV in the presence of an energy-independent barrier of transmission T [40]. If we look at the WTD of electrons transmitted through the scatterer, it displays a crossover from a Wigner-Dyson distribution at perfect transmission to an exponential at low transmission. Indeed, for a perfectly transmitting channel, in which the scattering state can be seen as a train of noninteracting fermions, the average waiting time in which electrons are separated is given by $\bar{\tau} = h/eV$. This separation is due to the Pauli exclusion and the statistical distribution is approximated by a Wigner-Dyson surmise.

$$\mathcal{W}(\tau) = \frac{32}{\bar{\tau}^3\pi^2}\tau^2 \exp\left[-\frac{4}{\pi}\frac{\tau^2}{\bar{\tau}^2}\right]. \tag{10}$$

This shape is easily understood by a mapping between one-dimensional fermions to random matrices of the Gaussian unitary ensemble [40]. Another important indicator of fermionic statistics is the fact that the WTD vanishes at $\tau = 0$. As T is reduced, the WTD spreads to longer waiting times and develops oscillations similar to Friedel oscillations with period h/eV. Close to pinch off ($T \ll 1$) WTD approaches an exponential distribution which is the signature of uncorrelated events. Indeed, in that case the detection time of scattered electrons is very long and conclusively detected electrons are no longer correlated. The mean waiting time is simply given by $\langle\tau\rangle = \bar{\tau}/T$, while the corresponding current reads $e/\langle\tau\rangle = \frac{e^2}{h}VT$, well known as the Landauer formula [64]. Another interesting benchmark is the case of a single channel with a resonant transmission of Lorentzian shape. If the applied voltage is larger than the width of the resonance, the WTD can be shown [40] to be well approximated by a function of the form $W(\tau) = \Gamma^2\tau\exp(-\Gamma\tau)$, with Γ a parameter linked to the width of the resonance (see Appendixes C and D for details). If several resonances are present in the voltage windows, oscillations in the WTD show up due to interferences between different energy paths [40].

IV. RESULTS

We present in this section the WTDs found for two different situations. First, we consider the setup in Fig. 1(a) without a Zeeman field ($\Delta_Z = 0$), hosting ABSs, and second with a Zeeman field lifting the Kramers degeneracy at the DP in the normal region. In the later situation MBS appear on the two interfaces between the superconducting and magnetic regions above a certain value of the Zeeman field, which induces a topological transition (see Appendix A for details). Our goal is to discuss the different effects between the two characteristic phases (trivial vs. topological) in terms of their WTDs and finally identify a possible distinction between the two.

A. Andreev bound states: $\Delta_Z = 0$

We begin with the study of a TRS Josephson junction by considering the system without a Zeeman field ($\Delta_Z = 0$). Following the BTK scattering formalism [63], we calculate the scattering probabilities for an incoming electron from the source (see Appendix A) with boundary conditions at $x = 0, L, L + L_m$ and $x = 2L + L_m$. To relate the scattering coefficients to the respective WTDs in detail, we first present in Fig. 2(a) the energy dependence (at $\phi = 0$) of the two coefficients $T_e(E) = |t_e|^2$ (blue) and $R_h(E) = |r_h|^2$ (red dotted), namely the probability that an incoming electron is transmitted as an electron or reflected as a hole. There, we find resonances with a energy difference $\Delta E \propto v_F/L_m$. The transmission probability $T_e(E)$ arises due to the structure of the junction, which can be seen as a Fabry-Pérot interferometer with the two SC regions acting as barriers [62]. After the transmission of an electron through the first barrier, multiple Andreev reflections within the region enclosed by the two SCs allow those resonances to appear, and are known as Andreev bound states. The shape of the peaks can be modulated by the choice of the SC regions, such that a rather short region ($L < \zeta_{SC}$, with the SC coherence length $\zeta_{SC} = v_{F,s}/\Delta$) broadens the spectra. The length of the normal region (L_m) modifies the energy distance (and the number of states) of states within the SC gap. The Andreev reflection $R_h(E)$ shows dips at the corresponding resonances, which follows directly from the normalization condition, $T_e(E) + R_h(E) = 1$. Next, we evaluate the WTD [Eq. (2)] for these processes and present in Fig. 2(b) the WTD, where an incoming electron gets Andreev reflected for several voltage windows ($V_+ > 0$). For small voltages (black line) the Andreev reflection is unity. Conclusively, the WTD of reflected holes is well approximated by a Wigner-Dyson distribution, given by Eq. (10). Note that the indicated reference time is chosen by $\bar{\tau}_\Delta = h/\Delta$, while the WTDs have their maximum around the mean waiting time $\langle\tau\rangle = \bar{\tau} = h/eV$. With increasing voltage (red dotted and blue dashed lines), the WTD remains a Wigner-Dyson distribution, since the dips in the reflection coefficient [see Fig. 2(a)] are negligibly small and the channel can be seen as a perfectly reflecting one. Since the scattering coefficient $R_h(E)$ tends to zero for $E \gg \Delta$, a further increase of the voltage would result in an effective smaller reflection within the full window, thus the WTD would evolve towards an exponential distribution (not shown).

More interesting are WTDs between transmitted electron for the resonances in the scattering coefficient $T_e(E)$. For a better understanding, we choose several V_+, such that we cover with each step one more resonance peak of the electron transmission [see blue resonances in Fig. 2(a)]. We highlight the results in Fig. 2(c) by presenting the WTDs for several numbers of the transmitting resonances. In analogy to the Fabry-Pérot interferometry, we find for two resonance (red line) oscillations in the WTD with a period dictated by the energy difference of the two states [40]. For an increasing number of resonances we find on top of those oscillations additional oscillations. Those smaller oscillations allow, in principle, a counting of the resonances within the applied voltage window V_+ and are interpreted as interference between different paths in energy space [40]. We find that the overall shape of the WTD changes abruptly as an additional resonance is included in the voltage window, which can be readily understood in terms of transport through a finite number of resonances as described analytically in Appendix D.

We conclude this section by discussing the phase dependence of the SC pairing potential for the scattering coefficients and the WTDs in the absence of a Zeeman field. The phase dependence of the electron transmission [for details see Appendix A, Fig. 6(a)] is due to the spin momentum locking and the assumption of a right moving, incoming electron only symmetric in energy [$T_e(E) = T_e(-E)$] for $\phi = n\pi$, with integer $n \in \mathbb{Z}_0$. Thus, depending on the applied voltage, the superconducting phase difference can either keep the number of included states fixed (voltage is exactly in the middle of two states), or changes it by ± 1 (voltage is above/below the middle of two states). Note, since we consider the long junction limit, the transmission resonances have a linear dependency and conclusively the phase does not change the period of oscillations. Concerning the WTD of Andreev reflected holes, it is almost unaffected by the superconducting phase ϕ.

So far we have studied the situation of a time-reversal symmetric system and have not specifically considered the zero-energy state at $\phi = \pi$. For a better understanding, we will then break the TRS and determine the characteristic features in the WTDs.

B. Ideal Majorana bound states: $\Delta_Z \neq 0$

In this section we elaborate the results of the WTDs across the topological transition from trivial ABS at finite energies to topological protected zero-energy MBS, localized in between or on the interfaces between the ferromagnetic and superconducting regions. The inclusion of a finite Zeeman field Δ_Z lifts the Kramers degeneracy at the DP and splits the spin degenerated states into their spin up/down components, such that the TRS is broken and normal electron reflection (with spin flip) is now allowed. The splitting is most pronounced for states at lower energy (at the DP, note that $\mu_{TI} = 0$). A stronger rise of the Zeeman field leads to the appearance of the nontrivial MBSs, where all other states get pushed to higher energies, while the zero-energy anomaly pushes the amplitude of $R_e(0)$ to unity. As a consequence, normal electron reflection $R_e(E)$ (with spin flip) is the major indicator for a topological transition. Note that the criterion for a phase transition in this type of setup depends on the effective length scales of the superconducting and magnetic regions [65]. Furthermore, since both transmission probabilities (t_e, t_h) start to vanish with increasing Δ_Z, we calculate the WTDs for the transport channels of normal reflected electrons. As before, we first present the electron reflection $R_e(E)$ for an increasing Zeeman field in Fig. 3(a) at energies within the SC gap and without phase difference $\phi = 0$.

For the corresponding signal in the WTD we choose an energy window of -0.15Δ to 0.15Δ for three values of Δ_Z [see the bars in Fig. 3(a)]. The resulting WTDs for $\phi = 0$ are shown in Fig. 3(b). There, we find for $\Delta_Z = 0.1\Delta$ (black line) an oscillatory behavior in the WTD, since the applied voltage

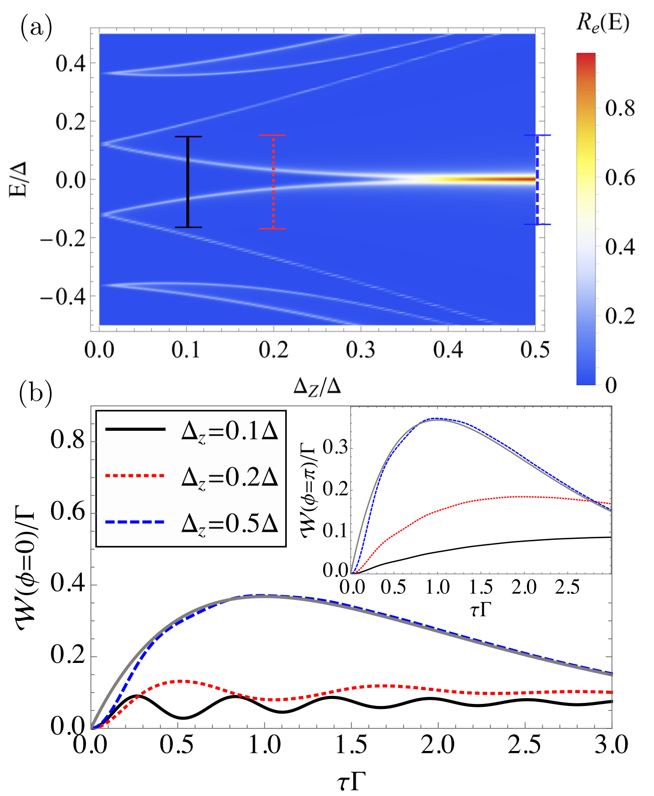

FIG. 3. (a) Scattering coefficient $R_e(E)$ depending on E and Δ_Z at $\phi = 0$. The colored bars indicate the measured energy window used in (b), where the respected WTDs of reflected electrons are presented. The grey line denotes the analytical result for the rate equation (see Appendix C). The inset shows the results for $\phi = \pi$. The rest of the parameters are those from Fig. 2 and $\Gamma = 0.077\Delta$.

window includes the two lowest-energy states [see the corresponding black line in Fig. 3(a)]. The period of the oscillations is proportional to the energy distance of the two states and can be described by two shifted Lorentzian resonances (see Appendix D).

The increase of the Zeeman field to $\Delta_Z = 0.2\Delta$ [red dotted line in Figs. 3(a) and 3(b)] still covers the two states with a smaller splitting of the states and conclusively induces a slower period of the oscillations in the WTD. Most strikingly, in the topological phase, (here at $\Delta_Z = 0.5\Delta$) [blue dashed line in Figs. 3(a) and 3(b)] the oscillations in the WTD disappear and the latter is similar to the distribution of a single channel with a single resonance (see Appendix C). More precisely it is given by $W(\tau) = \Gamma^2\tau\exp(-\Gamma\tau)$ (see gray line) with a maximum at $\tau = 1/\Gamma$, while $\Gamma = 2\gamma\pi$ is proportional to the full width at half-maximum (2γ) of the resonance. Thus, for $\phi = 0$ the phase-transition from the nontopological to the topological situation changes the WTD from oscillatory to nonoscillatory behavior, which can be used as an alternative indication of the presence of a zero-energy MBS. Furthermore, we present in the inset of Fig. 3(b) the WTDs for the same values of Δ_Z at $\phi = \pi$ [see Figs. 6(b)–6(d) in Appendix A for details of the reflection coefficients]. There, the previous oscillations at $\Delta_Z = 0.1$ and 0.2Δ are barely visible, since the electron reflection amplitudes of the higher-energy states are negligibly small due to the lifted spin degeneracy of the ABSs at $E \neq 0$. The exceptional point of the phase transition at $R_e(0, \phi = \pi) = |\tanh(L_m\Delta_Z)|^2$ in turn, stays robust and is shifted to lower values of the threshold for Δ_Z [see Appendix A, Fig. 7 and Eq. (A4)]. Conclusively, while the states for $\Delta_Z = 0.1\Delta$ and $\Delta_Z = 0.2\Delta$ are strongly phase dependent, the zero-energy states at $\Delta_Z = 0.5\Delta$ remains unaffected. Finally, we have checked (not shown) that intermediate values of the superconducting phase difference ϕ do not alter the picture established at $\phi = 0$ except for the precise location of the topological transition, which is ϕ dependent (this can be easily understood from the structure of the scattering coefficients displayed in Fig. 6 of Appendix A). Note that trivial ABSs at zero energy could possibly mimic those consequences imposed by a MBS, as it was shown in nanowires [29–36]. Due to the limitations of the model, we could not find such trivial states in the setup. To identify the mechanism to create the corresponding resonances in WTDs deserves additional investigation in order to present a clear distinction.

C. Nonideal Majorana bound states: $\Delta_Z \neq 0$

The previous results were calculated under ideal assumptions. We now discuss the effect of several parasitic ingredients that are inerrant to realistic experiments such as finite temperature, disorder or the influence of smooth interfaces on our findings. Details are given in Appendix B. We begin with the discussion of finite temperature in the leads, as well as in the SC. The finite temperature in the leads can be easily incorporated in the kernel as explained in Ref. [40]. We assume the temperature dependence in the superconducting potential following an approximated dependence [66],

$$\Delta(T) = \Delta\tanh\left(1.74\sqrt{\frac{T_c}{T} - 1}\right), \tag{11}$$

where the critical temperature is given by $k_B T_c = 0.568\Delta$. We focus on the trivial and topological WTDs [black and blue dashed line in Fig. 3(b)] and present them for increasing temperature in Fig. 4. In both cases, the WTD evolves smoothly from the ideal situation of Fig. 3 to a Wigner-Dyson distribution. This is simply attributed to the fact that, in both situations, the resonant states in between the two SC disappear because the system becomes effectively a single region with the corresponding Zeeman gap. As a consequence, electron reflection is perfect and therefore the stream of reflected electrons is described by Wigner-Dyson statistics. However, as long as the temperature remains smaller than about of few tens of percent of the critical temperature, the typical features discussed in the previous section remain visible.

Next, we include disorder into the Zeeman region, by cutting the region into N slices, each containing a constant Δ_Z and a chemical potential $\mu + \delta_\mu$, while δ_μ is from slice to slice Gaussian distributed with zero mean and the standard deviation σ_μ. Note, that we set $\mu = 0$, such that δ_μ acts as a critical disorder strength to destroy the topological phase. From that we can numerically evaluate the energy-dependent scattering coefficient $r_e(E)$, and then the WTD. We present in Figs. 5(a) and 5(b) the WTDs for three different disorder

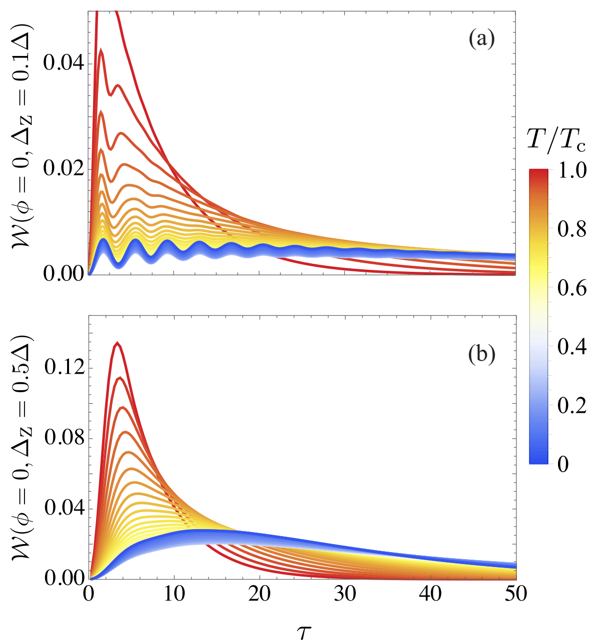

FIG. 4. WTDs of reflected electrons at finite temperature for the (a) trivial and (b) topological phase at $\phi = 0$. The color denotes lower (blue) and higher (red) temperatures.

strengths in the trivial and topological phase, respectively. Interestingly, in the trivial phase [Fig. 5(a)], the general distribution remains an exponentially decaying function, while the oscillatory part gets strongly affected by random resonances within the measurement window. In the topological phase [Fig. 5(b)], we find the expected WTDs that break down to the trivial one, when a disorder strength $\bar{\sigma}_\mu = \sqrt{N}\sigma_\mu > \bar{\sigma}_{\mu,\mathrm{crit}}$ is greater then the critical one. Thus, the WTD remains robust till the critical value of disorder $\bar{\sigma}_{\mu,\mathrm{crit}}$.

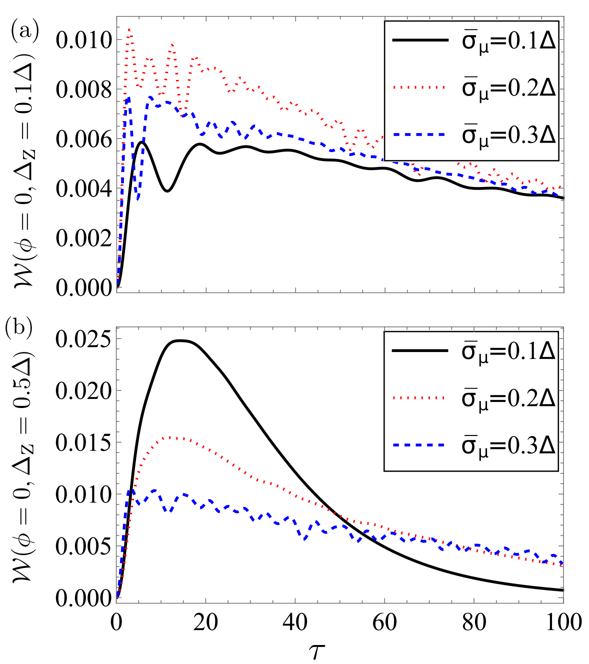

FIG. 5. WTDs of reflected electrons for several disorder strength in the trivial (a), $\Delta_Z = 0.1\Delta$ and topological phase (b), $\Delta_Z = 0.5\Delta$, at $\phi = 0$. The critical disorder strength for $\Delta_Z = 0.5\Delta$ is approximately $\bar{\sigma}_{\mu,\mathrm{crit}} \approx 0.17\Delta$. We choose $N = 1000$.

Finally, we have also included the effect of a smooth variation of the superconducting order parameter at the interface. In Appendix B we show that the only effect that enters is a renormalization of the scattering region length, which has no consequences on the qualitative picture but only slightly modifies the periods of oscillations in the WTD. Since trivial zero-energy states in nanowires can potentially arise from a specific shape of the electrostatic potential $\mu(x)$ in the normal part of the junction, the scattering coefficients in TI edge states remain, up to a phase, unaffected by such a potential.

V. SUMMARY AND CONCLUSION

In this paper we have calculated the WTDs associated to different scattering processes in a superconducting hybrid setup on quantum spin Hall edge states, proposed by Fu and Kane [8], across a topological transition.

At zero Zeeman field, in the topological trivial phase, TRS only authorizes two scattering processes, which are Andreev reflection and electron transmission. In the first case, we have shown that the WTD is well described by Wigner-Dyson statistics for any value of the applied voltage within the SC gap Δ. For the second scattering process, the electron transmission, the existence of resonances at finite energies in the scattering matrix, namely ABS resonances, induces specific oscillations in the WTD that we have described analytically within the formalism of Brandes [37].

Most importantly, we have then considered a finite Zeeman field in the area between the two superconducting islands, which is known to induce a topological transition between a trivial phase at low Δ_Z, characterized by the presence of ABS resonances in the scattering matrix, to a topological phase above a certain threshold where MBSs are present. Across this transition, we have focused on the WTD between reflected electrons (with spin flip), which is allowed by the breaking of TRS in the presence of a Zeeman field. We have shown that the WTD of reflected electrons displays an important qualitative change across the transition. In particular, the WTD has an oscillatory behavior (in time) in the trivial phase, with a strong Zeeman field dependence, which disappears in the topological phase. Importantly, this result is generic in terms of the superconducting phase difference except at the special point where $\phi = \pi$. However, in that specific case all ABS lying at energies greater than zero almost fully prohibits normal electron reflection, while the state at zero energy stays robust. The typical waiting time between reflected electrons in the topological phase is therefore unaffected while the one in the trivial phase diverges. Conclusively, a transition in the WTD is also visible in this specific case but with a strongly reduced threshold of the Zeeman field, which can be important in experimental implementations of this physics. Finally, we have discussed the effect of several parasitic ingredients such as disorder or finite temperature in the system. However, our study is limited to rather long junctions where both ABSs and MBSs resonances have the peculiarity to be well defined and well separated in both real space and energy. For short junctions they may overlap and blur the signature in the WTDs.

Since the model neglects bulk states of the TI, it was shown that in quantum well setups the DP is energetically located in the bulk of the TI. In such a situation we promote a different geometry of the heterostructure, where the magnetic field affects only the edges of the TI [61]. Additional limitations of the model prohibit the creation of trivial zero-energy ABSs [28], such that we would like to initiate future investigations on WTDs that consider the effects of scattering channels in detail by comparing trivial ABSs at zero energy and MBSs within other heterostructures [29–36].

We would like to conclude with a practical application of our setup. Experimental setups of topological Josephson junctions already have been studied in the literature [15,67,68]. Depending on the material realization of the two-dimensional TI different SCs have been used. If the WTD is not yet a routinely measured quantity, many progresses toward single-electron measurements are promising [49–55,58] and the WTD has been already measured in several experiments [54,56,57].

APPENDIX A: SCATTERING COEFFICIENTS

In this Appendix we explain details of the BTK formalism for the calculations of the scattering coefficients. In general, we consider a N-S-F-S-N junction as explained in the main text. The full scattering state is composed out of five parts, given by

$$\begin{aligned}\psi_{\mathrm{I}}(x) &= \vec{\mathbf{e}}_1 e^{ikx} + r_e \vec{\mathbf{e}}_2 e^{-ikx} + r_h \vec{\mathbf{e}}_4 e^{ikx},\\ \psi_{\mathrm{II}}(x) &= \sum_{i=1}^{4} a_i \vec{\mathbf{u}}_i e^{ik_i x},\\ \psi_{\mathrm{III}}(x) &= \sum_{i=1}^{4} b_i \vec{\mathbf{v}}_i e^{ik'_i x},\\ \psi_{\mathrm{IV}}(x) &= \sum_{i=1}^{4} c_i \vec{\mathbf{w}}_i e^{ik_i x},\\ \psi_{\mathrm{V}}(x) &= t_e \vec{\mathbf{e}}_1 e^{ikx} + t_h \vec{\mathbf{e}}_3 e^{-ikx},\end{aligned} \tag{A1}$$

where the eigenstates ($\vec{\mathbf{u}}_i$, $\vec{\mathbf{v}}_i$, $\vec{\mathbf{w}}_i$) are those of the Hamiltonian for the corresponding region and the vectors $\vec{\mathbf{e}}_i$ in the outer normal N regions are the four-dimensional Euclidean basis vectors of Eq. (1). The continuity conditions, according to the setup, must hold and allow us to calculate all coefficients of the scattering states, especially the transmission and reflection coefficients. The explicit conditions read

$$\begin{aligned}\psi_{\mathrm{I}}(0) &= \psi_{\mathrm{II}}(0),\\ \psi_{\mathrm{II}}(L) &= \psi_{\mathrm{III}}(L),\\ \psi_{\mathrm{III}}(L+L_m) &= \psi_{\mathrm{IV}}(L+L_m),\\ \psi_{\mathrm{IV}}(2L+L_m) &= \psi_{\mathrm{V}}(2L+L_m),\end{aligned} \tag{A2}$$

where the two outer wave functions (I and V) are those of the bare edge states, containing the necessary reflection (in ψ_{I}) and transmission (in ψ_{V}) coefficients. We have chosen the structure in such a way that the superconducting regions II and IV both have the length L, while the magnetic region III has length L_m. In general the scattering coefficients are complex.

Without Zeeman field we get the expression

$$\begin{aligned}r_h &= \frac{(-1+e^{2iL\Omega_\Delta})(-1+e^{i(2EL_m+\phi)})(-v^2+u^2 e^{2iL\Omega_\Delta})}{D},\\ t_e &= \frac{(u^2-v^2)^2 e^{-2iL(E-\Omega_\Delta)}}{D},\\ D &= u^2 v^2 (-1+e^{2iL\Omega_\Delta})^2 e^{i(2EL_m+\phi)}\\ &\quad + (u^2 e^{2iL\Omega_\Delta} - v^2)(u^2 - v^2 e^{2iL\Omega_\Delta}),\end{aligned} \tag{A3}$$

where $\Omega_\Delta = \sqrt{E^2-\Delta^2}$ and $u^2(v^2) = (E \pm \sqrt{E^2-\Delta^2})/\Delta$. For the more complex situation of a nonzero Zeeman field in the middle region, the results are to cumbersome to present, such that we present the important coefficients $T_e(E) = |t_e|^2$ and $R_e(E) = |r_e|^2$ in Fig. 6. At zero energy the scattering coefficients can be simplified to

$$\begin{aligned}r_e &= -\frac{2i\sinh(2L_m\Delta_Z)}{D},\\ r_h &= \frac{2\sin(\phi)\sinh(2\Delta L) - i(\cos(\phi)+1)\sinh(4\Delta L)}{D},\\ t_e &= \frac{4\cosh(L_m\Delta_Z)(\cosh^2(\Delta L) + e^{-i\phi}\sinh^2(\Delta L))}{D},\\ t_h &= \frac{2(1+e^{i\phi})\sinh(2\Delta L)\sinh(L_m\Delta_Z)}{D},\\ D &= \cosh(4\Delta L)[1+\cos(\phi)] + 2\cosh(2L_m\Delta_Z)\\ &\quad + [1-\cos(\phi)].\end{aligned} \tag{A4}$$

Within the main text, we use the change in the normal electron reflection from zero to unity as indicator for the topological phase transition (see Fig. 7).

APPENDIX B: SCATTERING COEFFICIENTS IN THE NONIDEAL SITUATION

We present in this Appendix first the effects of smooth pairing potentials (SC gap Δ or Zeeman field Δ_Z) and then by the inclusion of a disordered Zeeman region. Similar calculations have been made in Ref. [65]. The spatial arrangements of Δ and Δ_Z are chosen to have a ferromagnetic region enclosed by two superconducting regions, such that we assume first a steplike $\Delta(x) = \Delta[\Theta(x) - \Theta(x-L)] + \Delta e^{i\phi}[\Theta(x-L-L_m) - \Theta(x-2L-L_m)]$ and $\Delta_Z(x) = \Delta_Z[\Theta(x-L) - \Theta(x-L-L_m)]$. Without loss of results, we assume here $\phi = 0$ and $\mu = 0$ (μ will be included later), such that in terms of Pauli matrices the Hamiltonian reads

$$H(x) = -i\partial_x\tau_0\sigma_3 + \Delta_Z(x)\tau_3\sigma_1 - \Delta(x)\tau_2\sigma_2. \tag{B1}$$

To solve the scattering problem, we must calculate

$$H(x)\psi(x) = E\psi(x), \tag{B2}$$

which can be written in terms of the Pauli matrices

$$\begin{aligned}\partial_x\tau_0\sigma_3\psi(x) &= i(E - \Delta_Z(x)\tau_3\sigma_1 + \Delta(x)\tau_2\sigma_2)\psi(x)\\ \partial_x\tau_0\sigma_0\psi(x) &= i\tau_0\sigma_3(E - \Delta_Z(x)\tau_3\sigma_1 + \Delta(x)\sigma_2\tau_2)\psi(x)\\ \partial_x\psi(x) &= i(E\tau_0\sigma_3 - i\Delta_Z(x)\tau_3\sigma_2 - i\Delta(x)\tau_2\sigma_1)\psi(x).\end{aligned} \tag{B3}$$

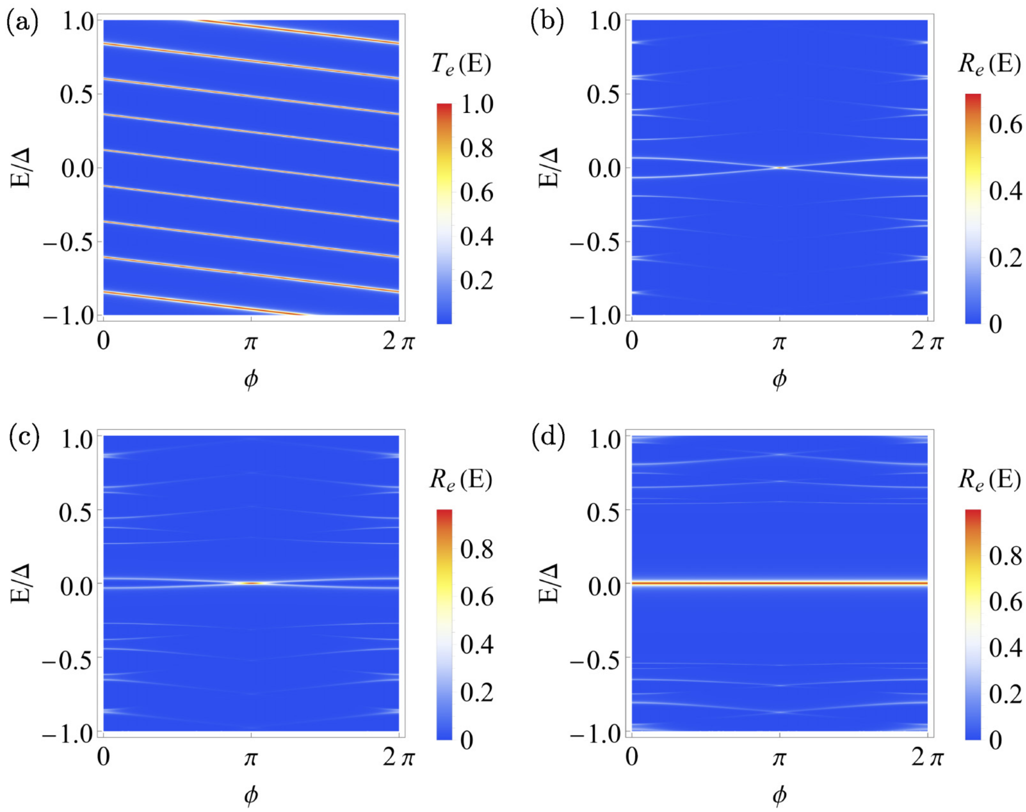

FIG. 6. Phase dependence of the scattering coefficient (a) $T_e(E)$ at $\Delta_Z = 0.0\Delta$, (b) $R_e(E)$ at $\Delta_Z = 0.1\Delta$, (c) $R_e(E)$ at $\Delta_Z = 0.2\Delta$, and (d) $R_e(E)$ at $\Delta_Z = 0.5\Delta$. The parameters are the same as in Fig. 2.

The solution of this first-order differential equation is formally given by

$$\psi(x) = U(x, x')\psi(x'), \quad U(x, x') = S_{\leftarrow} e^{i\int_x^{x'} dy h(y)}, \quad \text{(B4)}$$

where $S_{\leftarrow}$ is a spatial ordering operator, which arranges the spatial dependence of $h(y)$ from the right to the left. The operator $U(x, x')$ can be seen as a scattering matrix propagating through every region and connects the corresponding wave functions on the interfaces of the different regions.

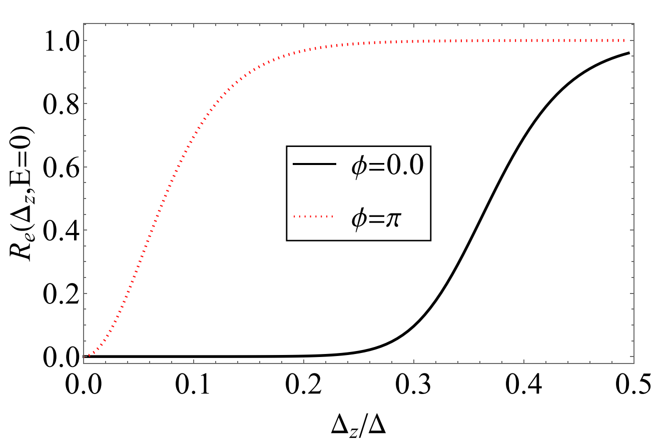

FIG. 7. Scattering probability of normal electron reflection at zero energy for $\phi = 0$ and $\phi = \pi$. We use the change of the normal electron reflection from zero to unity as indicator for the topological phase transition. The parameters are the same as in Fig. 2.

For the setup used in the paper, we are left with

$$\psi(2L + L_m) = U(2L + L_m, L + L_m)U(L + L_m, L) \times U(L, 0)\psi(0). \quad \text{(B5)}$$

The first operator, acting on $\psi(0)$, reads

$$U(L, 0) = \exp\left[i\int_L^0 dy(E\tau_0\sigma_3 - i\Delta(y)\tau_2\sigma_1)\right] \quad \text{(B6)}$$

$$= \exp[-iL(E\tau_0\sigma_3 + i\Delta\tau_2\sigma_1)], \quad \text{(B7)}$$

and results in an $L\Delta$ dependence (the ratio of the region length and the SC coherence length). Instead of an abrupt (Heaviside) change in $\Delta(x)$, we assume a smooth potential, given by

$$\Delta(x) = \Delta \tanh\left(\frac{x}{\lambda}\right) \tanh\left(\frac{L - x}{\lambda}\right), \quad \text{(B8)}$$

where Δ is the SC bulk gap, $x \in (0, L)$ and λ is an adjustment parameter on which the gap spatially changes on the interfaces at $x = 0$ and $x = L$. Thus, by using the exponential representation of tanh, a substitution and a partial integration, the integral in Eq. (B4) becomes

$$\int_L^0 dy\Delta(y) = \Delta\left[L - 2\lambda \coth\left(\frac{L}{\lambda}\right) \log\left(\cosh\left(\frac{L}{\lambda}\right)\right)\right],$$

which describes that the shape of the potential is been covered by an effective length $L'(\lambda)$, depending on the adjustment parameter λ. In the same manner we find that the dependence of the other potential regions are the same (optionally with a different λ). Conclusively, the smoothness of the superconducting or Zeeman pairing potentials has the same influence as a change in the corresponding length of the region. In addition, the corresponding WTD does not show any unexpected discrepancies. Thus, we continue in the following with a stepwise change of the potentials.

Next we implement disorder within the Zeeman region, by including a spatially dependent chemical potential. We take from Eq. (B5) the operator within the Zeeman region, given by

$$U(L+L_m, L) = \exp\left[i\int_{L+L_m}^{L} dy(E\tau_0\sigma_3 - i\Delta_Z(y)\tau_3\sigma_2 + \mu(y)\tau_3\sigma_3)\right], \tag{B9}$$

and split this region into N slices, such that

$$\begin{aligned} U(L+L_m, L) &= \Pi_{i=1}^{N} U(L+L_{m,i}, L) \\ &= \Pi_{i=1}^{N} \exp\left[i\int_{L+L_{m,i}}^{L} dy(E\tau_0\sigma_3 - i\Delta_Z\tau_3\sigma_2 + \mu(y_i)\tau_3\sigma_3)\right], \end{aligned} \tag{B10}$$

while we explicitly neglect the spatial dependence of Δ_Z, since it is assumed to be constant. Taking the chemical potential $\mu(y_i) = \mu + \delta_{\mu,i}$, while $\delta_{\mu,i}$ is from slice to slice Gaussian distributed with zero mean and the standard deviation σ_μ and μ is assumed to be zero, we can evaluate numerically Eq. (B5) and calculate the corresponding scattering coefficients. We present in Figs. 8(a) and 8(b) the electron reflection coefficients for an increasing disorder strength at $\Delta_Z = 0.1\Delta$ and $\Delta_Z = 0.5\Delta$. Note that the standard deviation of a sum of N random independent variable scales with $1/\sqrt{N}$. We use in Fig. 5 in the main, such a disorder realization to calculate the WTDs.

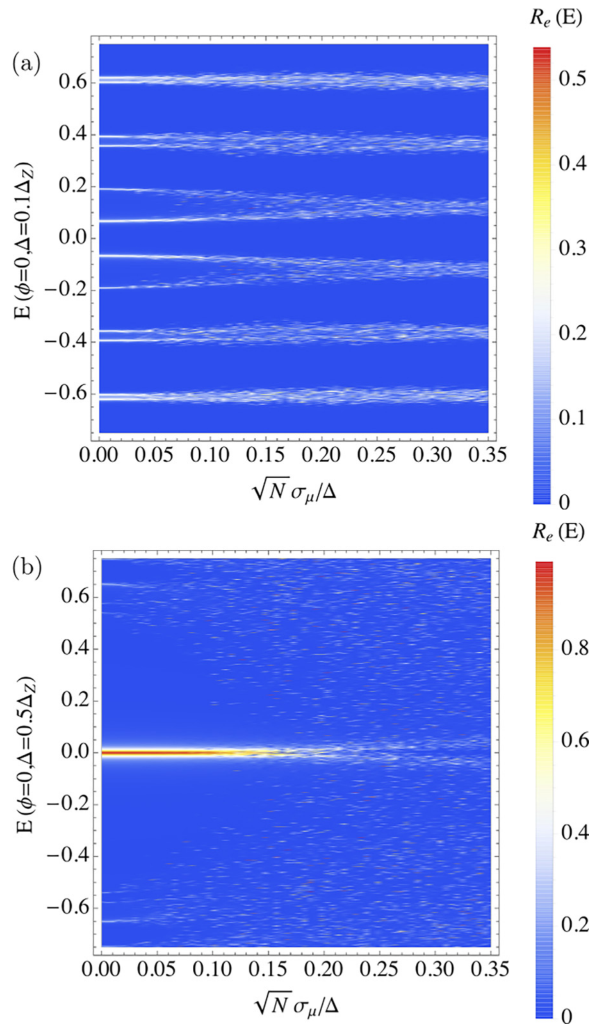

FIG. 8. Energy-dependent scattering probability of normal electron reflection for increasing disorder strength at $\phi = 0$. The parameters are the same as in Fig. 3(a), while we use $N = 1000$.

APPENDIX C: RATE EQUATION SINGLE DOT

We present in this Appendix the calculations for the rate equation for a double barrier following the results of Ref. [37]. Starting with the splitting of the Liouvillian

$$\mathcal{L} = \begin{pmatrix} -\Gamma_1 & 0 \\ \Gamma_1 & -\Gamma_2 \end{pmatrix} + \begin{pmatrix} 0 & \Gamma_2 \\ 0 & 0 \end{pmatrix} = \mathcal{L}_0 + \mathcal{J}, \tag{C1}$$

where $\mathcal{J} = |2\rangle\langle\bar{2}|$, with $\langle\bar{2}| = (0, \Gamma_2)$ and $|2\rangle = (1, 0)^\top$, measuring jumps from state 2 to 1. The corresponding WTD is given by

$$\hat{W}(z) = \langle\bar{2}|(z - L_0)^{-1}|2\rangle = \frac{\Gamma_1}{(z+\Gamma_1)}\frac{\Gamma_2}{(z+\Gamma_2)}, \tag{C2}$$

such that we get with the inverse Laplace transformation $F(z) = 1/(z+a) \to f(\tau) = e^{-a\tau}$,

$$W(\tau) = \frac{\Gamma_1\Gamma_2}{(\Gamma_1 - \Gamma_2)}(e^{-\Gamma_2\tau} - e^{-\Gamma_1\tau}) = \Gamma^2\tau e^{-\Gamma\tau}, \tag{C3}$$

while we assumed in the last step $\Gamma_1 = \Gamma_2 = \Gamma$ to derive the equation used in the main text of the paper. From

$$\frac{d^n W(\tau)}{d\tau^n} = (-1)^n e^{-\Gamma\tau}\Gamma^{n+1}(\Gamma\tau - n), \tag{C4}$$

the maximum of $W(\tau)$ is at $\tau = 1/\Gamma$.

APPENDIX D: WAITING TIME DISTRIBUTION FOR SERIES OF LORENTZIAN RESONANCES

In this Appendix we explain the derivation of the WTD for the inclusion of an arbitrary number of Lorentzian-shaped resonances. As explained in the main text, by including more than one resonance in the voltage window one finds an oscillatory behavior within the resulting WTD. In general, the distribution extend to waiting times much larger than h/eV, the typical time scale at which correlations between electrons or holes are important. We will then assume that the stochastic process can be reduced to a renewal process [40]. In that case, the WTD is related to the second-order correlation function or equivalently to the two-body density matrix of the field.

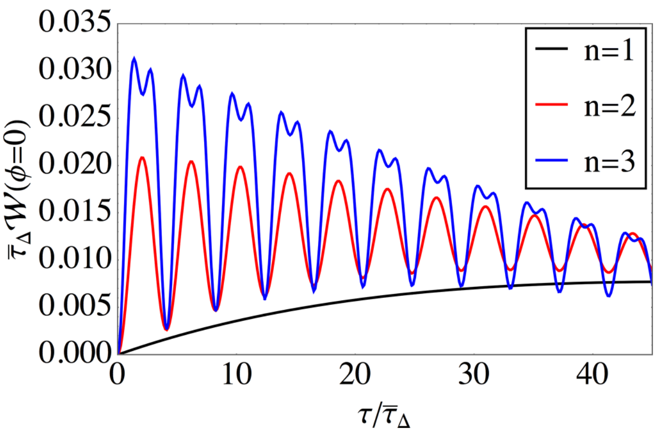

FIG. 9. Waiting time distributions for several numbers of resonance states. The parameters are given by the FWHM of the transmission coefficients for $\Gamma = 0.021\Delta$ and $\omega = 0.24\Delta 2\pi$.

In order to compute the second-order correlation function, we write the field operator in Fourier space,

$$\Psi_n^\dagger(x) = \int dk e^{ikx} a_{k,n}^\dagger, \tag{D1}$$

with n the number of resonances and $a_{k,n}$ the destruction operator in a plane wave, whose statistical properties will be given below. The resulting one-body density matrix $\rho_{1,n}$ is therefore given by

$$\begin{aligned}\rho_{1,n}(x,y) &= \langle \psi_n^\dagger(x)\psi_n(y)\rangle = \int dkdk' e^{i(kx-k'y)}\langle a_{k,n}^\dagger a_{k',n}\rangle \\ &= \int dkdk' e^{i(kx-k'y)}\left[\sum_{j=1}^n \frac{\delta_{k,k'} f(k)\gamma^2}{(k-jk_0)^2+\gamma^2}\right] \\ &= \int dk e^{ik(x-y)}\left[\sum_{j=1}^n \frac{\gamma^2}{(k-jk_0)^2+\gamma^2}\right] \\ &= \pi\gamma e^{-\gamma|x-y|}\left[\sum_{j=1}^n e^{ik_0 j(x-y)}\right],\end{aligned} \tag{D2}$$

where we assumed that the propagator is given by the sum of Lorentzian-shaped distributions with a maximum of unity, an equidistant separation of k_0 and γ being half of the full width at half-maximum. We assumed that these states are perfectly in the voltage window, such that the Fermi distribution $f(k)$ is unity. Next, we evaluate the two-body density matrix by using Wick's theorem, or equivalently by taking advantage of the fact that the field is described by a determinantal point process. This gives

$$\begin{aligned}\rho_{2,n}(x,y) &= \left|\begin{pmatrix}\rho_{1,n}(x,x) & \rho_{1,n}(y,x)\\ \rho_{1,n}(x,y) & \rho_{1,n}(y,y)\end{pmatrix}\right| \\ &= (\pi\gamma)^2\left(n^2 - e^{-2\gamma|x-y|}\left|\sum_{j=1}^n e^{ik_0 j(x-y)}\right|^2\right).\end{aligned} \tag{D3}$$

Going to the time domain by assuming a linear dispersion relation, we simply get

$$\tilde{\rho}_{2,n}(t,t') = (\pi\Gamma)^2\left(n^2 - e^{-2\Gamma|t-t'|}\left|\sum_{j=1}^n e^{iv_F k_0 j(t-t')}\right|^2\right), \tag{D4}$$

with the effective width $\Gamma = v_F\gamma$. The corresponding relaxation current [37] is then given by

$$\begin{aligned}I_n(t,t') &= I\frac{\tilde{\rho}_{2,n}(t,t')}{\tilde{\rho}_{2,n}(0,\infty)} \\ &= n\frac{\Gamma}{2}\left(1 - \frac{e^{-2\Gamma|t-t'|}}{n^2}\left|\sum_{j=1}^n e^{iv_F k_0 j(t-t')}\right|^2\right).\end{aligned} \tag{D5}$$

Since the process is stationary we may set $t = 0$ and $t' = t$. We then rewrite the absolute value of the sum of exponentials as

$$\left|\sum_{j=1}^n e^{iv_F k_0 j(-t)}\right|^2 = n + \sum_{j=1}^n 2(j-1)\cos[v_F k_0 t(n+1-j)], \tag{D6}$$

such that we have, for example,

$$I_1(t) = \frac{\Gamma}{2}(1 - e^{-2\Gamma|t|}) \tag{D7}$$

$$I_2(t) = \Gamma\left(1 - \frac{e^{-2\Gamma|t|}}{2}[1+\cos(v_F k_0 t)]\right). \tag{D8}$$

This further leads to three different types of standard Laplace transforms, namely

$$\int_0^\infty dt e^{-zt} = \frac{1}{z}, \tag{D9}$$

$$\int_0^\infty dt e^{-zt}\frac{e^{-2\Gamma t}}{n} = \frac{1}{n(z+2\Gamma)}, \tag{D10}$$

$$\begin{aligned}&\int_0^\infty dt e^{-zt}\frac{e^{-2\Gamma t}}{n^2}2(j-1)\cos[v_F k_0 t(n+1-j)] \\ &= \frac{2(j-1)(z+2\Gamma)}{n^2[(z+2\Gamma)^2+(\omega_j)^2]},\end{aligned} \tag{D11}$$

with $\omega_j = v_F k_0(n+1-j)$, it transforms the current to

$$I_n(z) = n\frac{\Gamma}{2}\left[\frac{1}{z} - \frac{1}{n(z+2\Gamma)} - \sum_{j=1}^n \frac{2(j-1)(z+2\Gamma)}{n^2[(z+2\Gamma)^2+(\omega_j)^2}\right]. \tag{D12}$$

To get the waiting time distribution, we assume a renewal process, which is justified if the typical waiting time is much larger than $\bar{\tau} = h/eV$. Following Ref. [37], we calculate

$$w_n(z) = \frac{I_n(z)}{1+I_n(z)}. \tag{D13}$$

The inverse Laplace transform is for $n > 1$ already difficult to handle. For example, the $n = 2$ WTD in Laplace space reads

$$w_2(z) = \frac{\Gamma(\omega^2(4\Gamma+z)+4\Gamma(2\Gamma+z)^2)}{\omega^2(4\Gamma^2+2z^2+5\Gamma z)+2(2\Gamma+z)^2(2\Gamma^2+z^2+2\Gamma z)}, \tag{D14}$$

with the inverse Laplace transformation

$$w_2(t) = \frac{1}{2\pi i}\int_{\alpha-i\epsilon}^{\alpha+i\epsilon} dz e^{tz}\frac{\Gamma(\omega^2(4\Gamma+z)+4\Gamma(2\Gamma+z)^2)/2}{(z-z_1)(z-z_1^*)(z-z_2)(z-z_2^*)}, \tag{D15}$$

with α a real number defining the so-called Bromwich contour. To calculate the contour, we evaluate the poles numerically. The structure of the poles is given by z_1, being close to the real axis containing a small imaginary part and result out of the term of the numerator with the highest power of ω ($\omega \gg \Gamma$). Further, depending on the number of resonances the rest of the poles contain a large imaginary part resulting in oscillations. We present in Fig. 9 the analytic results for the first three resonances.

Besides the great agreement to the numerical results, we find a difference in the damping of the oscillations, which might be accounted by deviations from the Lorentzian shape at higher energy within the model used in the main text [see Fig. 2(a)].

[1] C. W. J. Beenakker, Annu. Rev. Condens. Matter Phys. **4**, 113 (2013).
[2] C. Nayak, S. H. Simon, A. Stern, M. Freedman, and S. Das Sarma, Rev. Mod. Phys. **80**, 1083 (2008).
[3] B. A. Bernevig, T. L. Hughes, and S. C. Zhang, Science **314**, 1757 (2006).
[4] M. König, S. Wiedmann, C. Brüne, A. Roth, H. Buhmann, L. W. Molenkamp, X.-L. Qi, and S.-C. Zhang, Science **318**, 766 (2007).
[5] M. König, H. Buhmann, L. W. Molenkamp, T. Hughes, C.-X. Liu, X.-L. Qi, and S.-C. Zhang, J. Phys. Soc. Jpn. **77**, 031007 (2008).
[6] R. Skolasinski, D. I. Pikulin, J. Alicea, and M. Wimmer, Phys. Rev. B **98**, 201404(R) (2018).
[7] L. Fu and C. L. Kane, Phys. Rev. Lett. **100**, 096407 (2008).
[8] L. Fu and C. L. Kane, Phys. Rev. B **79**, 161408(R) (2009).
[9] J. Alicea, Rep. Prog. Phys. **75**, 076501 (2012).
[10] C. Schrade, A. A. Zyuzin, J. Klinovaja, and D. Loss, Phys. Rev. Lett. **115**, 237001 (2015).
[11] S. Hart, H. Ren, T. Wagner, P. Leubner, M. Mühlbauer, C. Brüne, H. Buhmann, L. W. Molenkamp, and A. Yacoby, Nature Phys. **10**, 638 (2014).
[12] S. Hart, H. Ren, M. Kosowsky, G. Ben-Shach, P. Leubner, C. Brüne, H. Buhmann, L. W. Molenkamp, B. I. Halperin, and A. Yacoby, Nature Phys. **13**, 87 (2017).
[13] E. Bocquillon, R. S. Deacon, J. Wiedenmann, P. Leubner, T. M. Klapwijk, C. Brüne, K. Ishibashi, H. Buhmann, and L. W. Molenkamp, Nature Nanotechnol. **12**, 137 (2017).
[14] J. Wiedenmann, E. Liebhaber, J. Kübert, E. Bocquillon, P. Burset, C. Ames, H. Buhmann, T. M. Klapwijk, and L. W. Molenkamp, Phys. Rev. B **96**, 165302 (2017).
[15] H. Ren, F. Pientka, S. Hart, A. Pierce, M. Kosowsky, L. Lunczer, R. Schlereth, B. Scharf, E. Hankiewicz, L. W. Molenkamp, B. Halperin, and A. Yacoby, Nature **569**, 93 (2019).
[16] I. Knez, R.-R. Du, and G. Sullivan, Phys. Rev. Lett. **109**, 186603 (2012).
[17] A. Kononov, S. V. Egorov, V. A. Kostarev, B. R. Semyagin, V. V. Preobrazhenskii, M. A. Putyato, E. A. Emelyanov, and E. V. Deviatov, JETP Lett. **104**, 26 (2016).
[18] A. Kononov, V. A. Kostarev, B. R. Semyagin, V. V. Preobrazhenskii, M. A. Putyato, E. A. Emelyanov, and E. V. Deviatov, Phys. Rev. B **96**, 245304 (2017).
[19] J.-P. Xu, C. Liu, M.-X. Wang, J. Ge, Z.-L. Liu, X. Yang, Y. Chen, Y. Liu, Z.-A. Xu, C.-L. Gao, D. Qian, F.-C. Zhang, and J.-F. Jia, Phys. Rev. Lett. **112**, 217001 (2014).
[20] M.-X. Wang *et al.*, Science **336**, 52 (2012).
[21] C. Huang *et al.*, ACS Nano **12**, 7185 (2018).
[22] A. Kononov, G. Abulizi, K. Qu, J. Yan, D. Mandrus, K. Watanabe, T. Taniguchi, and C. Schönenberger, Nano Lett. **20**, 4228 (2020).
[23] F. Lüpke, D. Waters, S. C. de la Barrera, M. Widom, D. G. Mandrus, J. Yan, R. M. Feenstra, and B. M. Hunt, Nature Phys. **16**, 526 (2020).
[24] B. Jäck, Y. Xie, J. Li, S. Jeon. B. A. Bernevig, and A. Yazdani, Science **364**, 1255 (2019).
[25] V. Mourik, K. Zuo, S. M. Frolov, S. R. Plissard, E. P. A. M. Bakkers, and L. P. Kouwenhoven, Science **336**, 1003 (2012).
[26] A. Das, Y. Ronen, Y. Most, Y. Oreg, M. Heiblum, and H. Shtrikman, Nature Phys. **8**, 887 (2012).
[27] M. T. Deng, S. Vaitiekénas, E. B. Hansen, J. Danon, M. Leijnse, K. Flensberg, J. Nygård, P. Krogstrup, and C. M. Marcus, Science **354**, 1557 (2016).
[28] E. Prada, P. San-Jose, M. W. A. de Moor, A. Geresdi, E. J. H. Lee, J. Klinovaja, D. Loss, J. Nygård, R. Aguado, and L. P. Kouwenhoven, Nature Rev. Phys. **2**, 575 (2020).
[29] G. Kells, D. Meidan, and P. W. Brouwer, Phys. Rev. B **86**, 100503(R) (2012).
[30] C. Moore, T. D. Stanescu, and S. Tewari, Phys. Rev. B **97**, 165302 (2018).
[31] F. Peñaranda, R. Aguado, P. San-Jose, and E. Prada, Phys. Rev. B **98**, 235406 (2018).
[32] T. D. Stanescu and S. Tewari, Phys. Rev. B **100**, 155429 (2019).
[33] J. Avila, F. Peñaranda, E. Prada, P. San-Jose, and R. Aguado, Commun. Phys. **2**, 133 (2019).

[34] C. Zeng, G. Sharma, T. D. Stanescu, and S. Tewari, Phys. Rev. B **102**, 205101 (2020).
[35] H. Pan and S. Das Sarma, Phys. Rev. B **104**, 054510 (2021).
[36] S. V. Aksenov, J. Phys.: Condens. Matter **34**, 255301 (2022).
[37] T. Brandes, Ann. Phys. (NY) **520**, 450 (2008).
[38] M. Albert, C. Flindt, and M. Büttiker, Phys. Rev. Lett. **107**, 086805 (2011).
[39] M. Albert, G. Haack, C. Flindt, and M. Büttiker, Phys. Rev. Lett. **108**, 186806 (2012).
[40] G. Haack, M. Albert, and C. Flindt, Phys. Rev. B **90**, 205429 (2014).
[41] P. Stegmann, B. Sothmann, J. König, and C. Flindt, Phys. Rev. Lett. **127**, 096803 (2021).
[42] W. Liu, F. Wang, and R. Liang, Appl. Sci. **10**, 1772 (2020).
[43] P. P. Hofer, D. Dasenbrook, and C. Flindt, Physica E **82**, 3 (2016).
[44] E. Potanina and C. Flindt, Phys. Rev. B **96**, 045420 (2017).
[45] M. Albert and P. Devillard, Phys. Rev. B **90**, 035431 (2014).
[46] S. Mi, P. Burset, and C. Flindt, Sci. Rep. **8**, 16828 (2018).
[47] M. Albert, D. Chevallier, and P. Devillard, Physica E **82**, 85 (2016).
[48] D. Chevallier, M. Albert, and P. Devillard, Europhys. Lett. **116**, 27005 (2016).
[49] N. Walldorf, C. Padurariu, A.-P. Jauho, and C. Flindt, Phys. Rev. Lett. **120**, 087701 (2018).
[50] J. Bylander, T. Duty, and P. Delsing, Nature (London) **434**, 361 (2005).
[51] F. D. Parmentier, E. Bocquillon, J.-M. Berroir, D. C. Glattli, B. Plaçais, G. Fève, M. Albert, C. Flindt, and M. Büttiker, Phys. Rev. B **85**, 165438 (2012).
[52] J. Dubois, T. Jullien, F. Portier, P. Roche, A. Cavanna, Y. Jin, W. Wegscheider, P. Roulleau, and D. C. Glattli, Nature (London) **502**, 659 (2013).
[53] E. Bocquillon, V. Freulon, J.-M. Berroir, P. Degiovanni, B. Plaçais, A. Cavanna, Y. Jin, and G. Fève, Science **339**, 1054 (2013).
[54] S. Singh, P. Menczel, D. S. Golubev, I. M. Khaymovich, J. T. Peltonen, C. Flindt, K. Saito, E. Roldan, and J. P. Pekola, Phys. Rev. Lett. **122**, 230602 (2019).
[55] M.-H. Bae, D.-H. Chae, M.-S. Kim, B.-K. Kim, S.-I. Park, J. Song, T. Oe, N.-H. Kaneko, N. Kim, and W.-S. Kim, Metrologia **57**, 065025 (2020).
[56] C. Flindt, C. Fricke, F. Hohls, T. Novotny, K. Netocny, T. Brandes, and R. J. Haug, Proc. Natl. Acad. Sci. USA **106**, 10116 (2009).
[57] N. Ubbelohde *et al.*, Nature Commun. **3**, 612 (2012).
[58] J. Basset, H. Bouchiat, and R. Deblock, Phys. Rev. B **85**, 085435 (2012).
[59] F. Crépin, B. Trauzettel, and F. Dolcini, Phys. Rev. B **89**, 205115 (2014).
[60] F. Keidel, P. Burset, and B. Trauzettel, Phys. Rev. B **97**, 075408 (2018).
[61] F. Schulz, K. Plekhanov, D. Loss, and J. Klinovaja, Phys. Rev. Res. **2**, 033215 (2020).
[62] H. van Houten and C. W. J. Beenakker, Phys. B: Condens. Matter **175**, 187 (1991).
[63] G. E. Blonder, M. Tinkham, and T. M. Klapwijk, Phys. Rev. B **25**, 4515 (1982).
[64] Y. M. Blanter and M. Büttiker, Phys. Rep. **336**, 1 (2000).
[65] C. Fleckenstein, F. Keidel, B. Trauzettel, and N. Traverso Ziani, Eur. Phys. J. Spec. Top. **227**, 1377 (2018).
[66] M. Kamp and B. Sothmann, Phys. Rev. B **99**, 045428 (2019).
[67] A. Fornieri, A. M. Whiticar, F. Setiawan *et al.*, Nature (London) **569**, 89 (2019).
[68] T. W. Schmitt, M. R. Connolly, M. Schleenvoigt, C. Liu, O. Kennedy *et al.*, Nano Lett. **22**, 2595 (2022).